

Birth and growth of a granular jetJohn R. Royer,¹ Eric I. Corwin,¹ Bryan Conyers,¹ Andrew Flior,¹ Mark L. Rivers,² Peter J. Eng,^{1,2} and Heinrich M. Jaeger¹¹*James Franck Institute and Department of Physics, The University of Chicago, Chicago, Illinois 60637, USA*²*Consortium for Advanced Radiation Sources, The University of Chicago, Chicago, Illinois 60637, USA*

(Received 1 December 2007; published 18 July 2008)

The interaction between fine grains and the surrounding interstitial gas in a granular bed can lead to qualitatively new phenomena not captured in a simple, single-fluid model of granular flows. This is demonstrated by the granular jet formed by the impact of a solid sphere into a bed of loose, fine sand. Unlike jets formed by impact in fluids, this jet is actually composed of two separate components, an initial thin jet formed by the collapse of the cavity left by the impacting object stacked on top of a second, thicker jet which depends strongly on the ambient gas pressure. This complex structure is the result of an interplay between ambient gas, bed particles, and impacting sphere. Here we present the results of systematic experiments that combine measurements of the jet above the surface varying the release height, sphere diameter, container size, and bed material with x-ray radiography below the surface to connect the changing response of the bed to the changing structure of the jet. We find that the interstitial gas trapped by the low permeability of a fine-grained bed plays two distinct roles in the formation of the jet. First, gas trapped and compressed between grains prevents compaction, causing the bed to flow like an incompressible fluid and allowing the impacting object to sink deep into the bed. Second, the jet is initiated by the gravity driven collapse of the cavity left by the impacting object. If the cavity is large enough, gas trapped and compressed by the collapsing cavity can amplify the jet by directly pushing bed material upwards and creating the thick jet. As a consequence of these two factors, when the ambient gas pressure is decreased, there is a crossover from a nearly incompressible, fluidlike response of the bed to a highly compressible, dissipative response. Compaction of the bed at reduced pressure reduces the final depth of the impacting object, resulting in a smaller cavity and in the demise of the thick jet.

DOI: [10.1103/PhysRevE.78.011305](https://doi.org/10.1103/PhysRevE.78.011305)

PACS number(s): 45.70.Cc, 47.56.+r, 83.80.Fg, 83.10.Tv

I. INTRODUCTION

The impact of a solid object into a granular bed is a common and seemingly simple event. However, though this phenomenon has been studied since the 18th century [1,2], it still contains many surprises and continues to provide new insight into the unusual nature of granular materials. Granular materials constitute a unique state of matter which can flow like a liquid yet also support weight like a solid [3]. Both of these properties are exhibited during impact since material will initially flow out of the way of the impacting object until the object can no longer overcome the resistance of the bed and is brought to rest. This suggests the potential of impact experiments to characterize general properties of granular materials. Particularly notable are a number of engineering studies in the early 1960s motivated by questions about the load-bearing capability of the lunar surface [4–7]. These studies typically focused on the penetration depth of the impactor, and found that this depth depends strongly on details that do not enter for impact into simple solids or liquids, such as the grain diameter, bed packing density, and ambient gas pressure. There have been a number of recent studies using low speed impacts to address related, unanswered questions in granular physics, such as how force is distributed through a granular pack [8,9] and the functional form of the drag force on an object moving through a granular bed [10–15].

In 2001 Thoroddsen and Shen performed experiments dropping a solid sphere into a loose, fine-grained granular bed and found a remarkable phenomenon. As reported in [16], the impacting sphere easily sinks into the loosely

packed bed. After an initial, coronalike splash, a collimated jet of sand is ejected upwards, reaching heights over 40 cm. This granular jet is very reminiscent of liquid jets [17–20], despite the absence of any strong cohesive forces keeping the grains together. Thoroddsen and Shen, in analogy to what might be expected for liquids, attributed the jet to the gravity-driven radial collapse of the cavity left behind the sphere. Arguing that the jet height was set by the sphere diameter, impact velocity, gravity, and an effective bed viscosity, they proposed a scaling relation for the jet height that collapsed their results for the measured range of grain diameter and release heights [16].

Subsequent experiments at the University of Twente, by Lohse and co-workers, studied the granular jets in more detail [21]. The Twente group also performed extensive simulations of quasi-two-dimensional particle-based systems and further developed the analogy to impact into a liquid via a hydrodynamic model. In this model the granular bed is treated as a simple fluid with hydrostatic pressure proportional to the depth. This pressure drives the walls of the cavity together until they collide at some depth below the surface with a diverging velocity, creating both upwards and downward jets along the vertical axis of symmetry. In [12] the Twente group focused on the bed properties, tracking the position of the sphere with a thin trailing thread attached as it descends through the bed and inferred the drag force on the sphere. Their results for a sphere released just above the surface could be fit by a simple drag force that depended linearly on the depth of the sphere below the surface. This drag force can be seen as arising from friction between the sphere and the bed, which is proportional to the hydrostatic pressure.

These previous experiments were all performed in open air at atmospheric pressure and only investigated aspects of the impact that were visible above the bed surface. They did not allow for direct visualization of the interior bed dynamics that lead to the formation of the jet. In the mechanism for jet formation proposed in [21] the ambient gas is limited to one aspect, namely that it introduces drag on the individual grains as they move out of the way of the impacting sphere. This leads one to expect a slightly larger jet in the absence of air. However, experiments by our group at reduced pressure reveal a dramatic decrease in the jet height [22]. For an ambient pressure $P_0 < 70$ kPa we found that the jet is actually composed of two stages, an initial thin jet followed by a sharp shoulder and a shorter thick jet. The height of the thick jet decreases with pressure until it is no longer observed below about 4 kPa, while the thin jet remains unchanged down to the lowest accessed pressure of 2 kPa. In order to image the initial stages of jet formation below the surface, high speed x-ray imaging was used to track the motion of the descending sphere and subsequent collapse of the cavity walls. These x-ray images at atmospheric pressure revealed a large pocket of air trapped below the surface which drove up the sand above it, creating the thick jet.

Granular jet formation has recently attracted the interest of the plasma physics community with the possibility of using these jets as a way to inject a large amount of dust particles into plasma [23]. Bulychev *et al.* have constructed an apparatus to generate granular jets in vacuum and plasma, though they have focused on enhancing the small jet obtained in vacuum by changing the shape of the impacting object [23,24].

The change in jet structure at reduced pressure is accompanied by a global change in the response of the bed. Despite the substantial amount of work studying the motion of a solid object moving through a granular medium [4–15,21,25], and with the exception of the engineering studies in the early 1960s [4–7], the role of the gas pressure has been largely ignored. Gas-grain interaction has been previously studied in fluidized beds [26], where a granular bed is subjected to a continuous, externally imposed gas flow or rapid vibration. However, in this case it is simply the initially quiescent, interstitial gas that changes the dynamics. Recent work by the Twente group [27] and our recent x-ray studies [28] have begun to address this issue. Both sets of experiments find a monotonic decrease in both the rise of the top surface of the bed during impact and the final depth reached by the sphere at reduced gas pressure. The Twente group attributes the reduced drag at higher gas pressure to local fluidization of the bed around the sphere, while our x-ray work finds that the bed as a whole behaves more like an incompressible fluid at high pressure but compacts below the sphere at reduced pressure.

The detailed role of gas pressure also has remained unresolved as far as the formation of the jet is concerned. In [27] the Twente group performed their experiments at reduced pressure using smaller spheres and release heights than in previous studies and did not observe the second, thick jet. They attribute the decrease in jet height at reduced pressure to the decreased penetration depth of the sphere and suggest that the thick jet is not generic but instead due to nearby

container walls. Finally, the role of the grain diameter and the scaling for the jet height found in [16] also requires re-examination in light of the role of the gas pressure. In order to address these open questions about the role of the bed properties, container boundaries and the gas pressure in jet formation, it is important to investigate the dynamics in the bed interior as well as above the surface.

In this paper we present optical measurements above the bed surface varying the sphere diameter, release height, grain size, and interstitial gas as well as x-ray radiography below the surface at pressures from atmospheric pressure down to 0.7 kPa. This allows us to connect the dynamics below the surface to the structure of the jet. Our results show that interstitial gas assists the formation of the jet both indirectly by mediating a more fluidlike flow of the bed, and, under certain conditions, directly by pushing sand upwards. We find that the jet structure does not depend sensitively on the container boundaries. The thick jet instead depends strongly on both the ambient pressure and the sphere diameter. The scaling proposed in [16] does not collapse our results, but instead we find that, at atmospheric pressure, the jet energy scales with the kinetic energy of the sphere at impact for a range of sphere sizes and release heights. As the pressure is decreased, the energy transferred to bed motion and jet decreases, reflecting the increased dissipation during compaction of the bed.

In Sec. II we describe the different experimental setups used for optical measurements above the bed and x-ray radiography below the bed. Section III presents the results of our measurements. We discuss these results in Sec. IV in light of Darcy's law for the flow of gas through a granular bed and conclude in Sec. V.

II. EXPERIMENTAL SETUP

A. Measurements above the bed surface

For optical measurements of the jet above the bed surface, a steel sphere was dropped into a 22 cm deep bed of spherical glass beads (MoSci Corp., grain diameter $d = 53 \pm 9$ μm , density $\rho_b = 2.5$ g/cm^3) in a cylindrical tube with a 14 cm inner diameter. The sphere diameter D_s was varied from 0.6 to 2.25 cm, and the release height H_{drop} varied from 110 to 2 cm (See Fig. 1).

As described in [12,21,27], before each drop the bed was aerated from below by dry nitrogen entering through a diffuser built into the bottom of the container. After slowly turning off the nitrogen flow, the bed would reproducibly settle into a low-density state. We estimate the packing density $\phi = V_g / V_{\text{tot}}$, where V_g is volume occupied by grains and V_{tot} is the total volume of the bed, to be about 0.55 after aeration in this large container. The system could be sealed and evacuated to reach ambient pressures P_0 as low as 0.15 kPa. The flow rate to the pump was limited to prevent air from bubbling up and disturbing the loose packing. Slowly cycling the pressure from atmospheric pressure down to 0.15 kPa and back before releasing the sphere did not change the dynamics of the jet, so we can safely conclude that the evacuation process did not disturb the loose packing of the bed. We checked for electrostatic charging by perform-

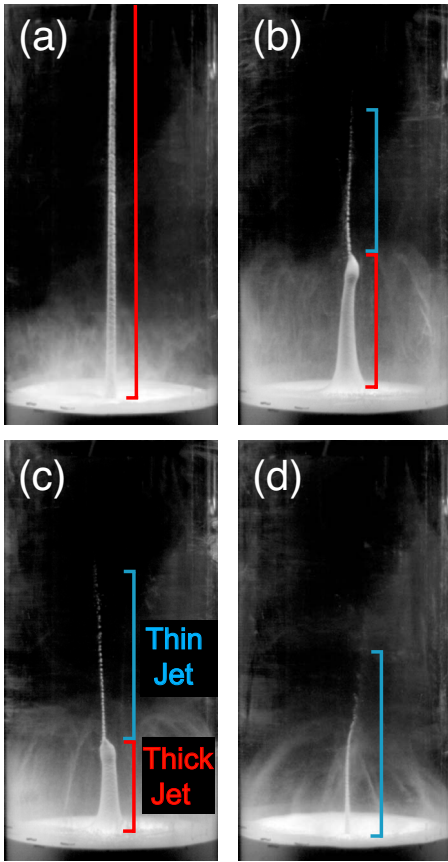


FIG. 1. (Color online) Granular jets at different ambient air pressures. Frames show the maximum height of the jet formed by a 2.25-cm-diameter steel sphere dropped from 1.1 m at pressures of (a) 101 kPa, (b) 26.7 kPa, (c) 13.3 kPa, and (d) 2.6 kPa. The thick and thin components of the jet are labeled by red and blue sidebars, respectively. At 101 kPa the thick jet extends out of the frame and obscures the thin jet. The bed particles in (a)–(d) were 53- μm -diameter glass beads and the packing density was ~ 55 .

ing experiments in air at a high level of relative humidity ($\sim 50\%$) where electrostatic effects typically vanish [29] and observed no qualitative change in the impact dynamics.

The sphere was held above the surface at the desired height by an electromagnet mounted to the top of the container. After the bed was aerated and the chamber evacuated to the desired pressure, the sphere was released and the impact was recorded with a Phantom v7.1 high-speed camera. After each drop the sphere was retrieved using a permanent magnet at the end of a long rod and the experiment was reset. The high-speed videos were analyzed to obtain quantities such as the maximum jet height and the rise of the bed. For all plots presented here, error bars correspond to statistical variations from five or more realizations of the experiment under identical conditions.

We also performed experiments in a sulfur hexafluoride (SF_6) atmosphere instead of ambient air in order to examine the role of the gas density. To ensure that all the air was replaced with SF_6 , the chamber was first evacuated below 3 kPa, and then SF_6 was let into the chamber to bring the pressure back to atmospheric level. The bed was subsequently aerated from below as in the other experiments, us-

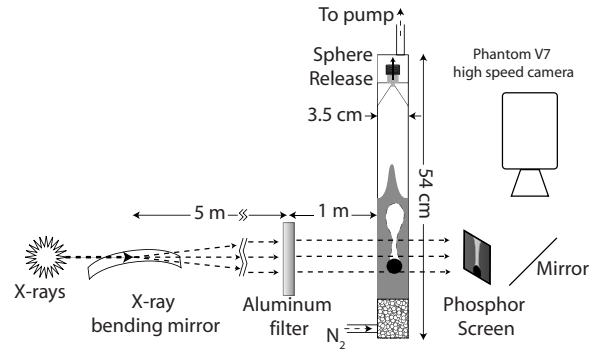


FIG. 2. Schematic of the x-ray setup. The x-ray bending mirror spread the beam and sets the high energy cutoff of 25 keV. The aluminum filter sets the low energy cutoff of 20 keV. The sphere release mechanism consisted of a conical holder with a permanent magnet which held the sphere centered in the holder. A solenoid was used to pull the magnet up and release the sphere.

ing SF_6 in place of nitrogen, then sealed and pumped down to the desired pressure.

To investigate jet formation in larger grains, a 11.4-cm-diameter sphere (a 12lb shot put) was dropped into a steel drum filled with corncob grounds with an average grain diameter of about 1 mm. The drum was 57 cm in diameter and filled 87 cm deep. The corncob grounds (density $\rho_b \sim 0.7 \text{ g/cm}^3$) ranged in size from 0.8 to 1.4 mm and were rough and nonspherical. The bed was too permeable to aerate because of the large grain diameter, so it was prepared in a loosely packed state by rapidly pouring the grains into the drum. The drops were performed in the stairwell of a five story building, allowing us to reach drop heights up to 27 m.

B. X-ray radiography

X-ray imaging of the interior of the bed was done at the University of Chicago GeoSoilEnviroCARS bending magnet beamline (13BMD) at the Advanced Photon Source using a high intensity beam with an energy width of 5 keV centered at 22.5 keV. A schematic of the x-ray setup is presented in Fig. 2. In order to obtain appreciable x-ray transmission through the bed, we were forced to use a thinner container and granular media with a lower atomic number. For the x-ray images presented here, spheres with $D_s = 1.2$ and 0.6 cm were dropped from 34 cm into a 8.5 cm deep bed of 50 diameter μm boron carbide (B_4C) particles. The bed was contained in a 3.5 cm inner diameter cylindrical polycarbonate tube with 1.6-mm-thick walls. Like the larger system, this chamber had a diffuser at the base to aerate the bed and could be sealed and evacuated down to as low as 0.7 kPa.

1. Image alignment

The local x-ray transmission through the bed was imaged off a phosphor screen at 6000 frames per second with resolution of 29 $\mu\text{m}/\text{pixel}$ using a Phantom v7 video camera. The beam size restricted the field of view to 22 by 8.7 mm^2 sections of the container. To capture the dynamics across the full vertical extent of the bed, movies of multiple independent drops, imaged at different, slightly overlapping vertical

bed positions, were stitched together using the passage of the sphere to align them horizontally and synchronize them. The chamber was mounted on a computer controlled translation stage, allowing us to precisely adjust the position of the chamber. The horizontal position of the tube was adjusted in 8.0 mm increments so that there was a 0.7 mm vertical overlap between adjacent movies. The horizontal and time offsets between adjacent movies were calculated by aligning the leading edge of the impacting sphere in the overlap region between frames. To align two adjacent movies, we first found the frame where the tip of the impacting sphere reached the bottom of the frame in the upper movie. Maximizing the cross-correlation between the overlap of the two movies, by varying time (frame number) and horizontal position, we obtained a horizontal shift and time offset for each movie. In Fig. 3 we illustrate this procedure using two adjacent movies taken inside the bed. This process was automated using batch routines written in IDL to produce offset tables for each set of movies at a given pressure. To produce a composite movie, each movie was reduced in size by binning into 8 pixel \times 8 pixel blocks, then assembled into a full column using the calculated offset table.

2. Calibration

The detector was calibrated pixel by pixel to convert intensity to packing density. The measured intensity, I , reaching the detector is a function of the product $\rho_b \phi l$. Here ρ_b is the density of the grain material and l the x-ray path length through the bed, as determined from the cylindrical geometry of the setup. The density of the B_4C particles is $\rho_b = 2.5 \text{ g/cm}^3$, identical to glass. Calibration curves relating I to the packing fraction ϕ were calculated for each of the 780×300 pixels in the field of view. This was done by filming a moving wedge of packed B_4C in a container with walls identical in thickness and composition to the cylindrical tube. This allowed us to empirically measure $I(\rho_b \phi l)$ for each pixel at fixed ρ_b and $\phi = 0.6$. This technique allowed us to simultaneously correct for spatial variation in beam intensity and fixed pattern noise on the camera's complementary metal-oxide-semiconductor (CMOS) image sensor [30]. From these empirical calibration curves we then generated lookup tables for each pixel giving ϕ vs I for fixed l in the cylindrical geometry.

The initial packing density ϕ_0 was calculated by averaging 100 frames taken before the sphere was released. At each pixel $\phi(t)$ fluctuated by about 0.5% due to camera noise. Prior to impact, the initial packing fraction ϕ_0 varied by about 1% across the frame, indicating a very high uniformity of the bed configuration prior to impact. From drop to drop ϕ_0 varied between 0.49 and 0.53. This variation in ϕ_0 was present at atmospheric pressure, where the pump was disconnected, as well as at reduced pressure, indicating that it was due to small, unavoidable differences in bed settling after fluidization, but not due to the evacuation of the chamber.

3. Flow tracing

For some x-ray experiments, a small number of $d \sim 100 \mu\text{m}$ potassium iodide (KI) particles were added to

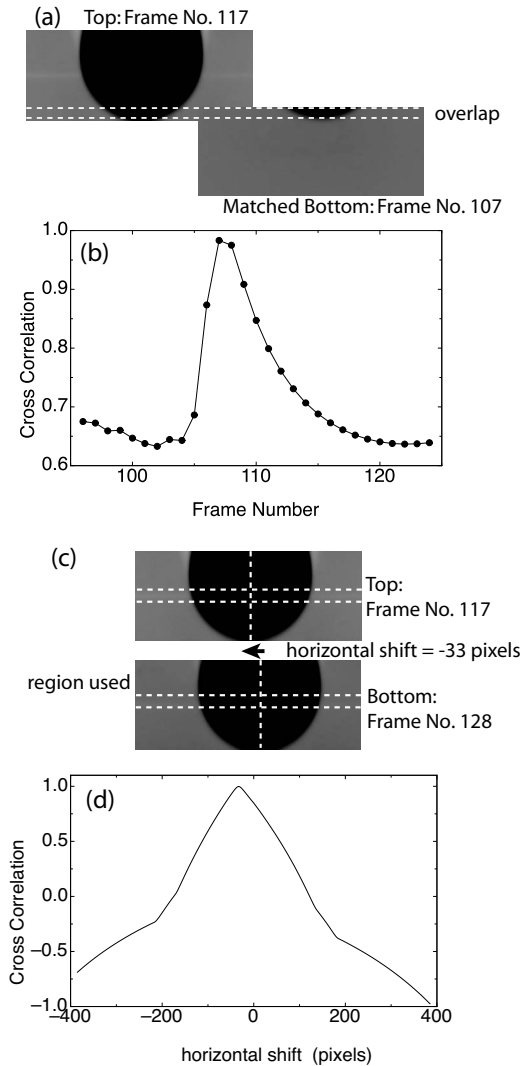


FIG. 3. Alignment of x-ray movies taken at different heights. Time alignment: (a) Stills from x-ray movies at 12 kPa showing the frames used to align radiographs filmed 72 mm (upper) and 64 mm (lower) from the bottom of the frame to the bottom of the bed. (b) Cross-correlation between fixed upper frame and varying lower frames across the region of overlap to determine time offset. (c) Images from the same upper/lower movies used to align radiographs horizontally. (d) Cross correlation for the fixed upper frame and varying amounts of shift for the lower frame to determine horizontal offset.

the bed. Due to iodine's higher atomic number these particles appeared darker in the x-ray images. They were added in small enough concentrations so only a few particles were visible in the frame, allowing us to track individual particles. Despite the difference in size and density of these particles, the overall bed dynamics did not change, and we can take the tracks of the KI particles as representative of the granular flow field in the bed.

4. Container size

The smaller container used in the x-ray experiments could possibly effect the formation of the jet. In order to examine the effects of the boundary, we performed experiments vary-

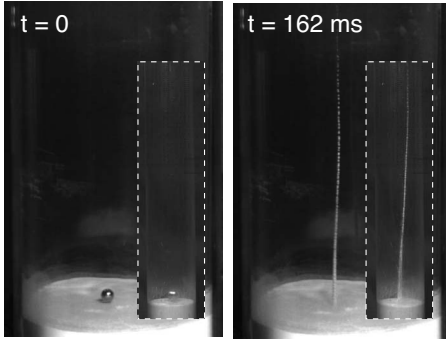


FIG. 4. Effect of boundaries. Jet formation in a 14-cm-diameter container filled 22 cm deep and in a 3.5-cm-diameter container filled 8.5 cm deep (outlined insets). For both cases $D_s=1.0$ cm, $H_{\text{drop}}=35$ cm, and the bed material was $53 \mu\text{m}$ glass spheres. The images for the big and small container have the same horizontal and vertical scales, and the insets are shifted such that the impact points of the sphere and the bases of the two jets line up.

ing both the bed depth and container size. In Fig. 4 we show still images from the jet formed when a $D_s=1$ cm sphere was dropped from 34 cm into $d=53 \mu\text{m}$ glass spheres contained in the large 14-cm-diameter container filled 22 cm deep and the smaller 3.5 cm diameter container filled 8.5 cm deep used in the x-ray experiments. Even though the boundaries were much closer to the sphere in the small tube, the resulting jets are essentially identical.

III. RESULTS

A. Above the bed surface

In this section we present our measurements taken above the surface for a range of parameters including sphere diameter, release height, grain size, gas density, and gas pressure. After impact the sphere sinks into the bed, creating a crown-shaped splash of grains and causing the bed's top surface to rise. The jet emerges from within the cavity created by the impacting sphere. As the jet rises, there is a velocity gradient along the height of the jet, creating a straining flow from top to bottom and ending with the break up of the jet into discrete clumps of grains.

1. Atmospheric pressure

In Fig. 5 we show our measured jet heights varying the sphere diameter D_s from 2.25 to 0.6 cm and varying the drop height H_{drop} from 110 to 1 cm at atmospheric pressure. These data are compared to previous measurements by Thoroddsen and Shen [16] and Lohse *et al.* [12,21]. Lohse *et al.* dropped a $D_s=2.5$ cm steel sphere into $d=40 \mu\text{m}$ non-spherical sand prepared with a very loose initial packing of $\phi_0=0.41$. Despite the different bed material, our measurements of the jet height H_{jet} fall on top of their results when scaled by the sphere diameter [Fig. 5(b)]. Thoroddsen and Shen dropped a $D_s=1.34$ cm lead sphere into beds of sand with different grain sizes d ranging from 80 to 275 μm . Though their measured jet heights in the 80 μm sand are comparable to jets observed here and in Ref. [21], for larger

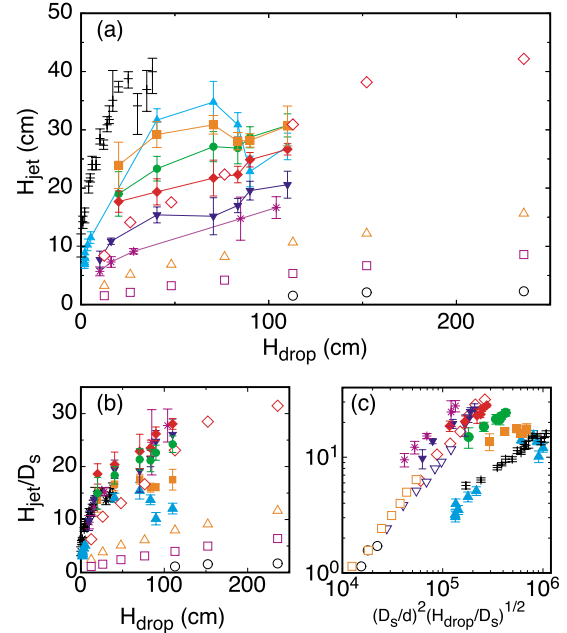


FIG. 5. (Color online) Comparison to previous work. (a) Maximum height of the thick jet vs drop height for different sphere diameters $D_s=2.25$ cm (\blacktriangledown), 1.75 cm (\blacksquare), 1.2 cm (\bullet), 1.0 cm (\blacklozenge), 0.8 cm (\blacktriangledown), and 0.6 cm ($*$) in a bed of $d=50 \mu\text{m}$ sand. Also plotted are previous results from Lohse *et al.* [21] ($+$) $D_s=2.5$ cm, $d=40 \mu\text{m}$ and Thoroddsen and Shen [16] $D_s=1.34$ cm, $d=80 \mu\text{m}$ (\diamond), 118 μm (\triangle), 176 μm (\square), and 25 μm (\circ). (b) Thick jet height scaled by the sphere diameter plotted vs drop height. (c) Rescaled horizontal axis for the data in (b) according to the scaling proposed in [16].

grains they observe significantly shorter jets. Their proposed scaling relation $H_{\text{jet}}/D_s \propto (D_s/d)^2 (H_{\text{drop}}/D_s)^{1/2}$ did not collapse our results for varying D_s [Fig. 5(c)].

We can estimate the total potential energy in the jet from images of the jet at its maximum height. Images were thresholded and the radius r_i of the jet measured at each horizontal row of pixels. Assuming that the jet is locally cylindrical, the volume of each row is $V_i = \pi r_i^2 \Delta z$, where Δz is the height of the row. The potential energy in each row is then $E_i = \rho_b \phi V_i g z_i$, where z_i is the height of row i above the bed surface, $\rho_b=2.5 \text{ g/cm}^3$ is the density of the bed material, and we assume $\phi \sim 0.5$ for the packing density in the jet. The total energy in the jet E_{jet} is then calculated by summing E_i from all the rows. The base of the jet was typically obscured by sand on the walls of the container, so the potential energy in this section was estimated by extrapolating the radius of the jet back to the surface. When the jet reaches its maximum height, the base of the jet is already beginning to fall downward. We do not include this kinetic energy, so our method systematically underestimates the jet energy. However, since the bottom has only begun to fall and is moving slowly, this kinetic energy is estimated to be less than 10% of the total jet energy. In some experiments we could measure H_{jet} but could not obtain an accurate profile of the full jet; these trials are excluded in Fig. 6.

We find that the jet energies obtained in this way reasonably collapse for a sizeable range of D_s and H_{drop} when plot-

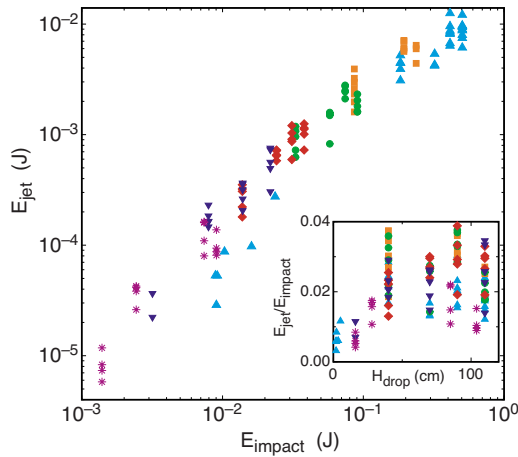


FIG. 6. (Color online) Energy transferred to the jet. Potential energy of the jet at atmospheric pressure is plotted against the kinetic energy of the sphere at impact. Sphere diameter $D_s = 2.25$ cm (\blacktriangledown), 1.75 cm (\blacksquare), 1.27 cm (\bullet), 0.95 cm (\blacklozenge), 0.79 cm (\blacktriangledown), and 0.6 cm ($*$). Inset: Ratio of jet potential energy to the spheres kinetic energy at impact vs release height.

ted against the kinetic energy of the sphere at impact E_{impact} (Fig. 6). The inset shows the ratio of E_j/E_{impact} is roughly constant to within a few percent for $H_{\text{drop}} \gtrsim 30$ cm, but decreases for lower drop heights.

2. Reduced pressure

The jets observed at reduced pressure are dramatically different from jets observed at atmospheric pressure. Figures 1(b)–1(d) show the jets formed by a $D_s = 2.25$ cm sphere released from $H_{\text{drop}} = 1.1$ m, each at the jet's maximum height. Below about 67 kPa a clear two-stage structure develops, consisting of an initial thin jet followed by a clear shoulder and a second, thicker jet. The height of the thick jet decreases with decreasing pressure until it is no longer observed below about 5 kPa. The remaining thin jet [Fig. 1(d)] is observed down to our lowest accessible pressure of 0.15 kPa. There is little change in the thin jet over this range of pressure even though at 0.15 kPa the gas mean-free path is comparable to the grain diameter and the Stokes drag a factor of 3 smaller than at 5 kPa. From this we conclude the thin jet is independent of the ambient gas and would continue to be observed as $P_0 \rightarrow 0$ [22].

As noted in [27], as the sphere diameter and release height are decreased the difference between the thick and thin jet becomes less distinct. In Fig. 7 we show images of the jet at $P_0 = 13.3$ kPa as D_s is decreased from 2.25 to 0.6 cm for $H_{\text{drop}} = 1.1$ m. The width of the thick jet decreases and the shoulder between the thick and thin jets becomes less pronounced with decreasing D_s , until there is no clear separation between the thin and thick jet below $D_s = 1.0$ cm.

3. Bed rise

The diminished jet at lower pressures is accompanied by a decrease in rise δh of the bed top surface (Fig. 8). For D_s

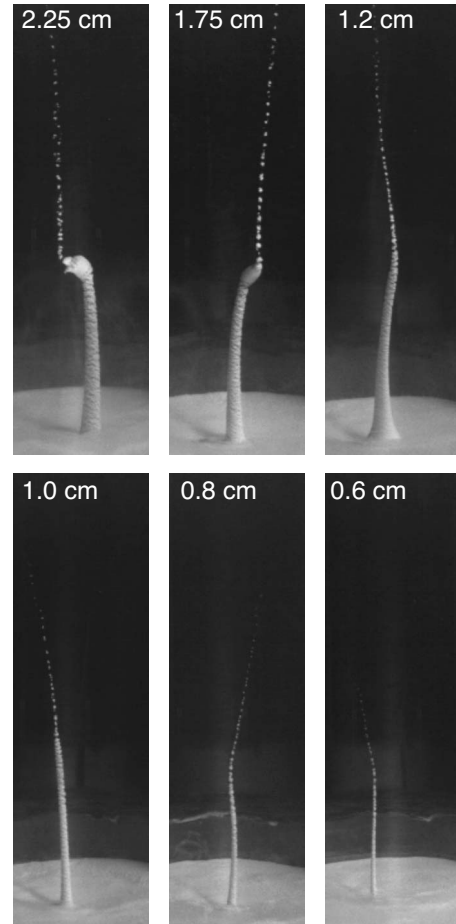


FIG. 7. Changing the sphere diameter. Images of the jet at its maximum height for $P_0 = 13.3$ kPa and $H_{\text{drop}} = 1.1$ m varying D_s from 2.25 to 0.6 cm.

$\gtrsim 1.0$ cm and $H_{\text{drop}} \gtrsim 40$ cm, the rise of the bed extends out to the container walls, allowing us to easily measure δh . We estimate the rise δh^* required for the packing density to remain constant by assuming that the sphere creates a cylindrical cavity extending to the bottom of the bed. For $D_s = 2.25$ cm and a 22 cm deep bed we calculate $\delta h^* \sim 0.6$ cm (denoted by the dashed red line in Fig. 8), which is consistent with the maximum rise of the bed δh_{max} at atmospheric pressure. As the pressure is decreased below about 60 kPa, δh_{max} decreases dramatically below δh^* , and the bed rises less than 0.1 cm at pressures below 3 kPa.

The lower δh_{max} at lower pressures implies that less energy from the impacting sphere is converted into potential energy of the bed. The inset in Fig. 8 shows the gravitational potential energy gained by the bed vs pressure, assuming uniform dilation of the bed. Even at atmospheric pressure, the energy transferred to the bed is almost an order of magnitude less than the kinetic energy of the impacting sphere. As the pressure is decreased, the energy transferred to the bed decreases to only a few percent of the impact energy. Even less energy goes into the jet. The jet's maximum potential energy is only a few percent of the impact energy at atmospheric pressure and further decreases with decreasing pressure to only a few hundredths of a percent below 3.5 kPa.

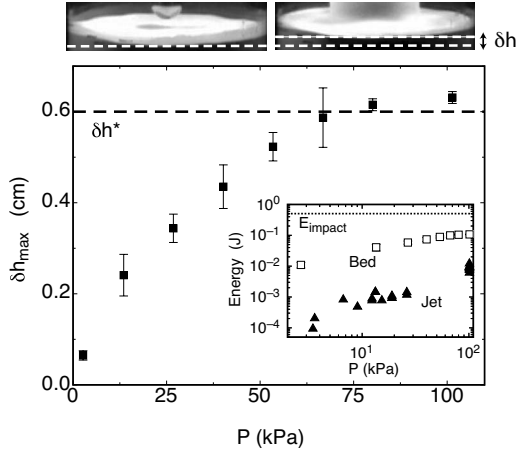


FIG. 8. Bed rise height vs ambient air pressure. Maximum rise height of the top surface of the sand bed measured at the side of the container using a 2.25 cm sphere released from 1.0 m. Images above the graph highlight the change in height δh . The dashed line marks rise height δh^* needed for a constant packing density, assuming a cylindrical cavity to the bottom of the container. Inset: Change in potential energy of the bed after falling from its maximum height to its final height (\square) and potential energy in the jet (\blacktriangledown). The dotted line denotes the kinetic energy of the impacting ball $E_{\text{impact}}=0.5$ J.

4. Larger grains

To investigate jet formation for larger grains, a 11.4-cm-diameter sphere (12 lb shot put) was dropped into a 57-cm-diameter steel drum filled 87 cm deep with $d \sim 1$ mm corncob pieces. Figure 9 shows the impact and jet formed for $H_{\text{drop}}=5.2$ m. We still observe a sharp, well-defined jet in the larger grains, but it is much smaller than one would predict if the jet height scaled with the other lengths in the system, as in the scaling proposed in [16]. If we scale D_s , H_{drop} , and d down by the same factor of 20, this would be comparable to a $D_s=0.6$ cm sphere dropped from $H_{\text{drop}}=26$ cm in $d \sim 50 \mu\text{m}$ spheres, where we measure $H_{\text{jet}} \sim 10$ cm (Fig. 5). The height of the small jet in Fig. 9(d), however, does not follow the same scaling. Instead of a 20×10 cm=200 cm jet in the larger system, the jet here reaches a maximum height of only 11 cm, roughly the diameter of the sphere.

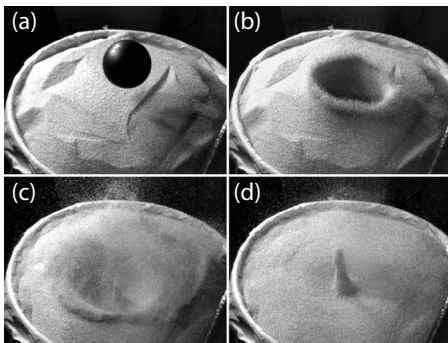


FIG. 9. Scaling up to large grains. Jet formation in $d \sim 1$ mm corncob pieces at times $t=(a)-7.3$ ms, (b) 23.3 ms, (c) 173 ms, and (d) 291 ms after impact of a $D_s=11.4$ cm shot put.

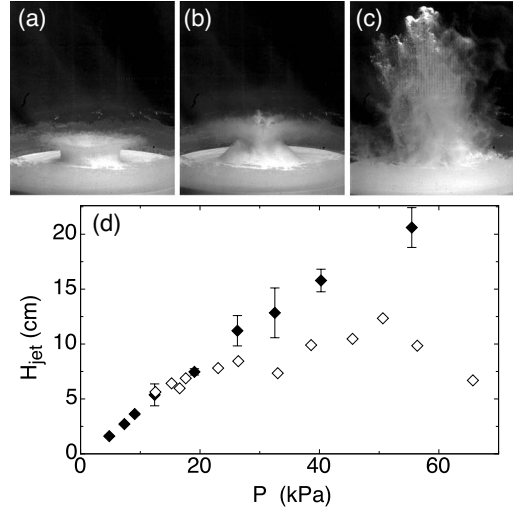


FIG. 10. Increasing gas density. Impact of a $D_s=2.25$ cm sphere released from $H_{\text{drop}}=1.1$ m with the ambient air replaced by SF_6 at $P_0=101$ kPa at times $t=(a)$ 12.5 ms, (b) 29.5 ms, and (c) 162 ms after impact. (d) Maximum height of the thick jet vs pressure in air (\blacklozenge) and SF_6 (\diamond). For SF_6 , $\rho_g=6.1$ g/m³ at $P_0=101$ kPa, $\mu=1.6 \times 10^{-5}$ Pa s, while for air $\rho_g=1.2$ g/m³ at $P_0=101$ kPa and $\mu=1.8 \times 10^{-5}$ Pa s.

5. Gas density

To examine the effect of the gas density ρ_g independently from the effect of air pressure, we performed drops in the 15-cm-diameter container using $d=53 \mu\text{m}$ grains with the ambient air ($\rho_g=1.2$ g/m³ at $P_0=101$ kPa, viscosity $\mu=1.8 \times 10^{-5}$ Pa s) replaced by sulfur hexafluoride (SF_6 , $\rho_g=6.1$ g/m³ at $P_0=101$ kPa, $\mu=1.6 \times 10^{-5}$ Pa s). At pressures below 25 kPa we found no difference between the jets in air and in SF_6 . Above 25 kPa in SF_6 , the corona from the initial splash was dragged inward and interfered with the rising jet and decreased its height. This effect, also noted in [21] at larger release heights, is due to the underpressure behind the sphere. This underpressure, which is proportional to $\rho_g v_s^2$, becomes more pronounced when either ρ_g or the sphere velocity v_s is increased. Above 70 kPa the underpressure was so pronounced that it prevented the formation of a focused jet, and instead only a violent eruption of gas and grains was observed [Figs. 10(a)–10(c)]. Increasing the impact velocity by increasing the drop height (up to 26 m in our experiments) produced the same inward collapse of the corona when the shot put impacted in the large 1 mm grains.

B. Below the bed surface

The experimental data obtained from measurements above the surface demonstrate that the ambient gas pressure plays a key role in the formation of the granular jet. In order to examine the interaction between the grains in the bed and the surrounding gas in more detail, we used high-speed x-ray radiography to capture the dynamics of the bed interior and measure local changes in the bed packing density.

1. Composite x-ray images

Figure 11 shows image sequences assembled from experiments conducted with a $D_s=1.2$ cm sphere dropped from

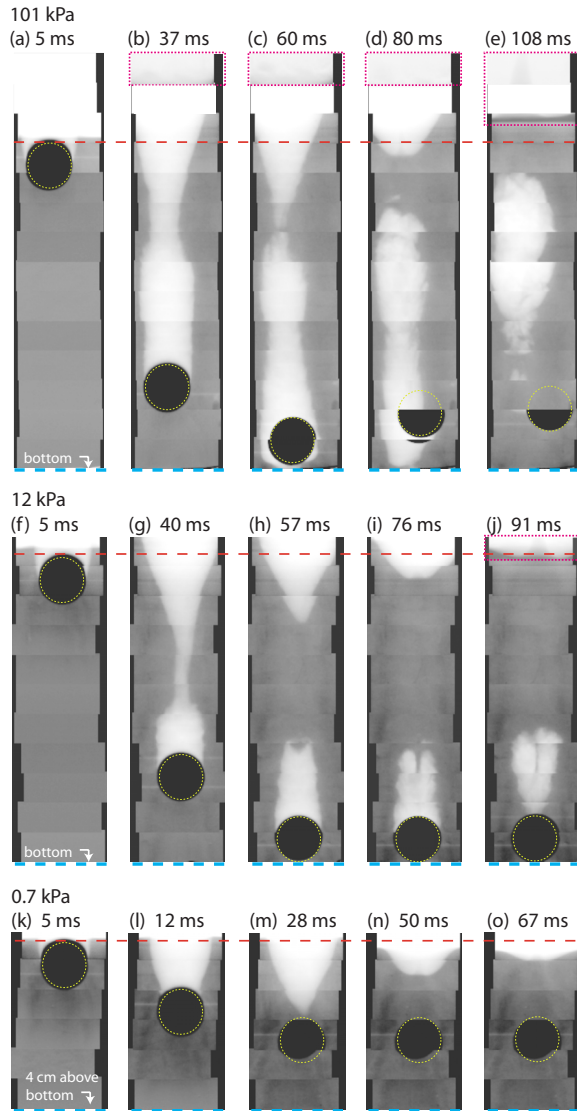


FIG. 11. (Color online) Composite x-ray images at (a)–(e) atmospheric pressure ($P_0=101$ kPa), (f)–(j) reduced pressure ($P_0=12$ kPa), and (k)–(o) vacuum ($P_0=0.7$ kPa) after impact of a $D_s=1.2$ cm sphere released from $H_{\text{drop}}=32$ cm. Time from impact labeled above each composite image. Dashed lines at the top of each image mark the top surface prior to impact. Dashed lines below each image mark the bottom of the bed in (a)–(j) ($P_0=101$ and 12 kPa) and 4 cm above the bottom of the bed in (k)–(o) ($P_0=0.7$ kPa). Contrast in boxed sections adjusted separately to highlight the top surface and jet. For movies see [31].

$H_{\text{drop}}=32$ cm into a 3.5-cm-diameter container at $P_0=101$, 12, and 0.7 kPa [31].

Images of the interior reveal the complicated dynamics below the surface that lead to the formation of the granular jet. At atmospheric pressure the sphere opens up a large cylindrical cavity [Fig. 11(b)]. As the sphere travels through the bed, the top surface rises until it reaches its maximum height about 30 ms after impact. The sphere reaches the bottom of the bed 50 ms after impact, hitting the bottom surface with enough momentum to bounce up a bit [Fig. 11(d)]. About 60 ms after impact the bed begins to fall back down. The walls of the cavity are driven inward by both the hydro-

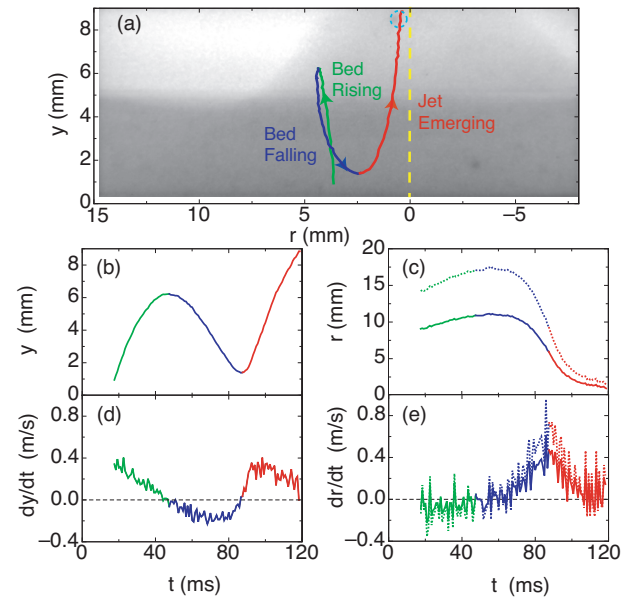


FIG. 12. (Color) Tracking a tracer particle. (a) Trajectory of a KI tracer particle $y(t)$ vs $r_m(t)$ overlaid on an image of the base of the jet 115 ms after impact. (b) Vertical position of the tracer $y(t)$ from (a). (c) Maximum (dotted line) and minimum (solid line) allowed radial trajectory computed assuming axisymmetric flow so that $r_m(t)=r_{\text{true}}(t)\cos\theta$. The requirement that the particle remain between the inner edge of the cavity and the wall of the container at all times determined the bound on θ : $66^\circ \leq \theta \leq 75^\circ$. Using the difference in the centerline of the jet and centerline of the sphere, we estimate the error in r from deviations from axisymmetric flow to be ~ 1.5 mm. (d) and (e) plot computed derivatives of (b) and (c), respectively. The tracer particle used to generate this track is highlighted by a dashed blue circle, and the centerline of the path of the sphere is denoted by the vertical dashed line.

static pressure and the momentum of the falling bed. The walls of the cavity pinch shut at two points, one at a depth $z_c=2.7$ cm below the initial top surface, and a second pinch-off just above the sphere. The upper pinch-off creates the thin upward jet as well as a small downward jet into the cavity. Most importantly, it traps a pocket of air in the lower portion of the cavity. The large hydrostatic pressure at the bottom of the bed continues to drive sand into the lower pinch-off, forcing the air pocket to close from the bottom. This rapid closure compresses the air pocket and drives the pocket upwards, erasing any downward jet [Fig. 11(e)]. While the air pocket is pushing upwards, the sand bed continues to fall, driving sand into the upper pinch-off. This sand is then pushed upward by the rising air pocket, forming the thick jet.

This is shown explicitly in Fig. 12 by following the path of a KI tracer particle situated slightly below the top surface of the bed. The particle initially rises with the bed but, as the bed falls, moves down and radially in toward the center of the cavity. About 80 ms after impact the particle rapidly changes direction again and moves up with the jet. Since x-ray radiography provides only a two-dimensional (2D) projection of the full three-dimensional (3D) bed, we cannot directly measure the true radial position of the particle $r_{\text{true}}(t)$ directly. In general the measured radial position $r_m(t)$ is re-

lated to the true position by $r_m(t) = r_{\text{true}}(t) \cos \theta$, where θ is the angle from the imaging plane. However, for axisymmetric flow θ is constant and $r_{\text{true}}(t)$ follows $r_m(t)$ up to a constant multiplicative factor. For the particular track in Fig. 12 we can bound $66^\circ \leq \theta \leq 75^\circ$ by requiring the particle to remain between the inner edge of the cavity and the wall of the container at all times. From the measured $y(t)$ and $r_m(t)$ we then compute the vertical and radial components of the particle's trajectory. As the particle moves down with the bed and in toward the center, its radial velocity increases, presumably due to the hydrostatic pressure of the bed [21]. When the particle is accelerated upward into the jet, its vertical velocity changes from 0.2 m/s downward to 0.4 m/s upward in less than 10 ms. This is especially rapid compared to the slow change of the radial velocity when the particle is inside the jet, which lasts for 25 to 35 ms.

Around 110 ms after impact the bed stops falling, and material no longer flows into the upper pinch off, ending the formation of the jet. The air pocket continues to rise, though much more slowly, and reaches the surface about 200 ms later, where it breaks the surface and violently erupts.

As the ambient pressure is lowered the dynamics below the surface begin to change. Figures 11(f), 11(i), and 11(j) show still images from a composite x-ray movie at $P_0 = 12$ kPa, where the thick jet is still observed but much smaller than the thick jet at atmospheric pressure. The sphere moves through the bed slower than at atmospheric pressure and the bed does not rise as high. The cavity walls pinch shut at a lower depth of $z_c = 4.1$ cm below the surface 40 ms after impact, while the sphere is still moving downward through the bed. This deeper pinch off creates an air pocket that is considerably smaller than the trapped air pocket at atmospheric pressure. The pronounced downward jet in Fig. 11(h) suggests that there is initially an underpressure in the cavity behind the sphere. The sphere reaches the bottom of the bed 60 ms after impact, 20 ms after the top of the cavity pinched shut. Because of this delay, the trapped air pocket is much smaller, and a thin upward jet has already formed from the inertial collapse of the cavity [Fig. 11(i)]. In Figs. 11(i) and 11(j) we see that this smaller air pocket closes up from the bottom and pushes the top of the pocket up, as at atmospheric pressure. As at 101 kPa, this closure compresses the air pocket and drives the top surface of the air pocket upward, erasing the downward jet and creating the thick jet [Fig. 11(j)].

As the pressure is further lowered, the sphere moves through the bed slower and the top surface of the bed rises even less. Figures 11(k)–11(o) show x-ray images at $P_0 = 0.7$ kPa, where the bed barely rises above its initial height and the sphere is stopped by the bed only 3.5 cm below the top surface. Here the cavity walls pinch shut at one point immediately above the sphere 28 ms after impact [Figs. 11(m)]. This inertial collapse of the walls creates a faint, thin jet [Figs. 11(n) and 11(o)].

2. Motion of the sphere through the bed

This change in jet formation process with pressure is the result of a dramatic change in the mechanical response of the sand bed. We examine this change using the x-ray video to

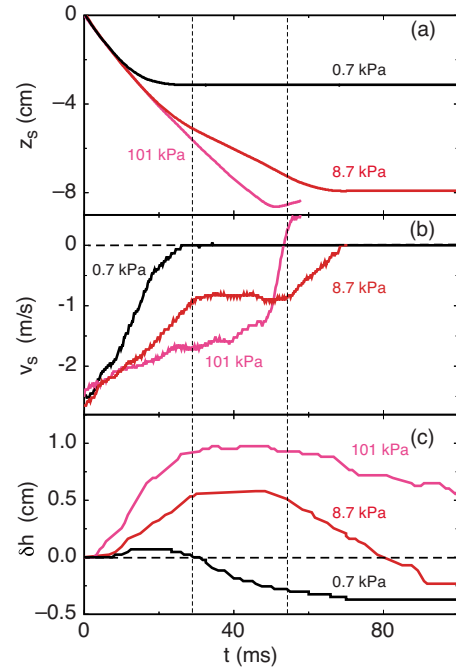


FIG. 13. (Color online) Motion of sphere and bed surface for $D_s = 1.2$ cm. (a) Vertical position z_s of bottom tip of the sphere as a function of time after impact (at $t = 0$ s). (b) Velocity $v_s(t)$ computed from curves in (a). (c) Rise of bed top surface. $D_s = 1.2$ cm.

simultaneously track the motion of the sphere, the global motion of the bed, and the local changes in bed packing.

In Fig. 13 we compare the motion of the sphere to the global rise of the bed. In Fig. 13(a) we track the position of the tip of the sphere $z_s(t)$ for different pressures. At $P_0 = 101$ kPa the sphere rapidly reaches the bottom and rebounds slightly, while at $P_0 = 8.7$ and 0.7 kPa the sphere is stopped before reaching the bottom. From these tracks we compute the sphere velocity $v_s(t) = dz_s/dt$ [Fig. 13(b)]. At intermediate pressures there is a constant velocity regime which begins about 30 ms after impact. This constant velocity regime is followed by a rapid deceleration of the sphere which occurs even at pressures where the sphere stops far above the bottom surface [28].

These dynamics cannot be captured by the simple depth- or velocity-dependent drag force laws proposed elsewhere [8, 11, 12, 15, 27], instead suggesting that the global motion of the bed is affecting the drag on the sphere. To compare the motion of the bed to the motion of the sphere, in Fig. 13(c) we plot the rise height of the top surface of the bed $\delta h(t)$ as a function of time. At impact, the bed rapidly rises, then levels off into a broad maximum highlighted by the vertical dashed lines.

This broad maximum in δh coincides with the constant velocity regime in $v_s(t)$. As described in [28], this suggests a scenario in which the concomitant reduction in drag results from a reduction in the Coulomb friction on the sphere. This Coulomb friction is set by the pressure exerted by the bed on the sphere. Assuming a simple hydrostatic pressure $\rho_b \phi g z$ this results in a drag force that increases linearly with depth [21, 15]. However, during the interval in which the broad maximum in δh is observed, the sphere is no longer driving

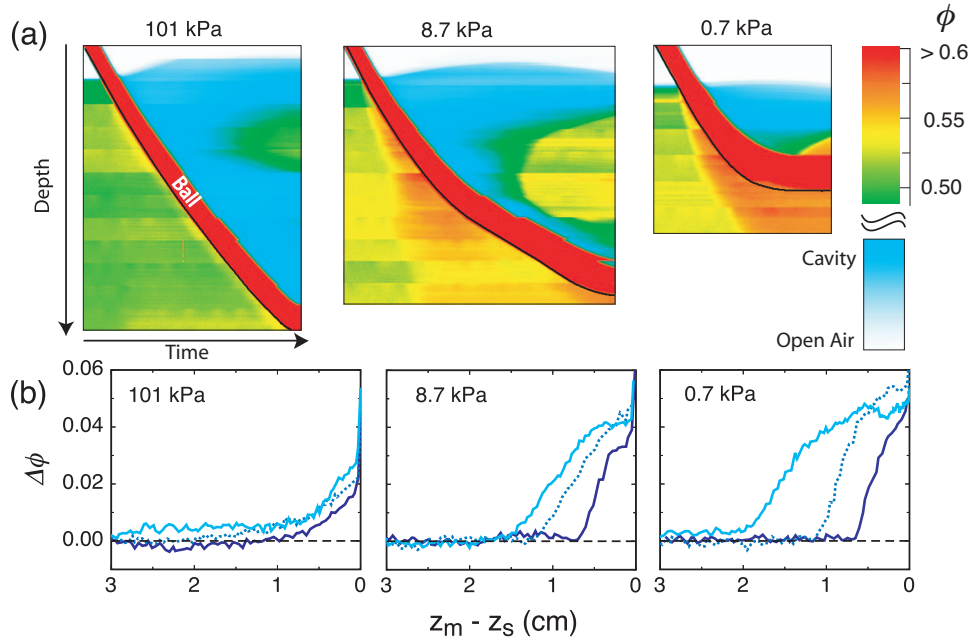


FIG. 14. (Color) Visualization of the compaction front that precedes the sphere at reduced pressure. (a) False color space-time plots of the centerline of the composite x-ray movies for three different pressures. Plots of the sphere position $z_s(t)$ from Fig. 13 are overlotted (black solid line) to indicate the boundary between the sphere (dark red) and the compacted sand in front of it. (b) Change in packing density $\Delta\phi = \phi - \phi_0$ measured along the centerline of the sphere path at fixed depths as the sphere is approaching. In each panel the three traces correspond to (from left to right) $z_m = 1.0, 2.0,$ and 3.0 cm. Data are plotted against the approach distance, i.e., the distance from the sphere bottom to z_m , so that $z_m - z_s = 0$ corresponds to the bottom of the sphere z_s arriving at depth z_m . At 101 kPa $\phi_0 = \{0.51, 0.51, 0.49\}$, at 8.7 kPa $\phi_0 = \{0.51, 0.52, 0.52\}$, at 0.7 kPa $\phi_0 = \{0.52, 0.51, 0.53\}$.

the bed up; instead bed material is falling into the cavity behind the sphere. As a consequence, the sphere only feels the weight of a small region around it [14] and can travel at nearly constant velocity. When the bed begins to fall again, the cavity behind the sphere has already pinched shut [Figs. 11(h) and 11(i)], trapping the air pocket below the surface [22]. Since material can no longer flow out of the way of the sphere, the pressure on the sphere, and hence the drag from friction increases dramatically and the sphere quickly decelerates to rest.

3. Impact-induced packing density changes

Figure 13(c) shows that the maximum change in height δh increases with pressure, suggesting that the bed as a whole is less compressible and more fluidlike in the presence of interstitial gas. In Fig. 14 we illustrate the connection between the rapid deceleration of the sphere and increased compaction of the bed at low pressures. In order to clearly see the compacted region below the sphere, we calculate space-time plots from the composite x-ray movies. These space-time plots show the time evolution of the packing density along the vertical centerline of the column. At $P_0 = 101$ kPa the packing density ϕ remains constant except for a small increase immediately ahead of the sphere. However, at $P_0 = 8.7$ and 0.7 kPa there is a jump in ϕ below the sphere. As the sphere moves through the bed, more material compacts below it and the leading edge of the compacted region moves further ahead of the sphere. This creates a front of compacted grains which moves through the bed *faster* than the sphere.

This is most evident at 8.7 kPa, where the leading edge of the front reaches the bottom of the bed 50 ms before the sphere comes to rest.

In Fig. 14(b) we plot the change in local packing density $\Delta\phi(t) = \phi(t) - \phi_0$ at three different depths z_m below the surface vs the distance to z_m measured from the approaching bottom tip of the sphere $z_s(t)$. After the initial compaction, the magnitude of $\Delta\phi$ at a given depth remains roughly constant in time, while the average magnitude of compaction increases with decreasing pressure [28].

4. Sphere diameter

Experiments with a smaller impacting sphere ($D_s = 0.6$ cm) [31] showed qualitatively similar behavior, except for two aspects: the motion through the bed is slower, and multiple cavity pinch-off locations are possible (Fig. 15). The 0.6 cm sphere descends much slower than the 1.2 cm sphere, gradually coming to rest at the bottom of the bed 80 ms after impact. The cavity walls first pinch shut 40 ms after impact, earlier than with the 1.2 cm sphere since the cavity diameter is smaller. The cavity closes while the sphere is still descending, resulting in an underpressure in the cavity behind the sphere. This underpressure pulls bed material into the cavity, creating ragged walls and, eventually, several small air pockets separated by plugs of bed material, as seen in Fig. 15(e).

The maximum rise of the top surface $\delta h_{\max} = 0.25$ cm is about 1/4 of the value for the 1.2 cm sphere, which is consistent with the rise needed to conserve volume without com-

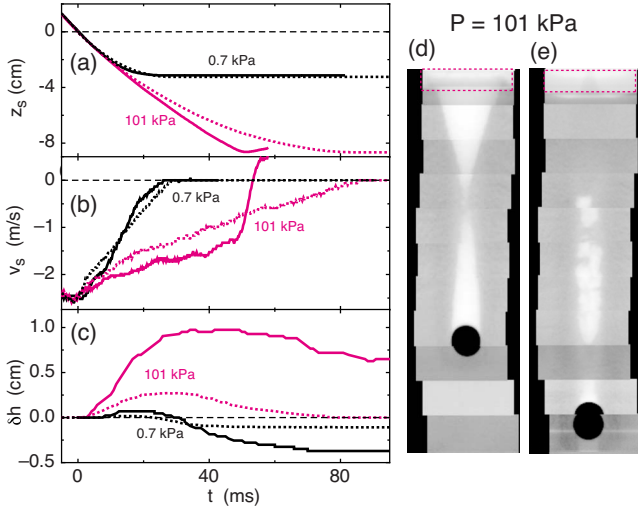


FIG. 15. (Color online) Effect of decreasing the sphere diameter. (a) Vertical position z_s of the bottom tip of the sphere, (b) computed velocity $v_s(t)$, and (c) rise of bed top surface at $P_0=101$ and 0.7 kPa. Dotted line: $D_s=0.6$ cm sphere. Solid line: $D_s=1.2$ cm. (d) and (e) are composite x-ray images of the cavity evolution for a $D_s=0.6$ cm sphere, (d) 39 ms and (e) 68 ms after impact at 101 kPa. Dashed lines in (a)–(c) denote the location of the top bed surface. Contrast in boxed sections of (d) and (e) adjusted separately to highlight the top surface. For movies see [31].

paction. For the 0.6 cm sphere, $\delta h(t)$ has a broad maximum similar to the 1.2 cm sphere, though it reaches this maximum much earlier and begins to fall while the sphere is still moving through the bed. The combination of the smaller rise of the bed and slower descent of the sphere leads to a smaller air pocket which cannot drive up the jet as vigorously as the larger air pocket formed by the larger sphere. Consequently, smaller overall jets result from smaller impacting sphere diameters (Fig. 7).

At reduced pressure with the $D_s=0.6$ cm sphere we see a compaction front and increased drag on the sphere similar to what we find for atmospheric conditions. However, despite the large difference between the trajectories for the two sphere diameters at 101 kPa, there is almost no difference at $P_0=0.7$ kPa [Figs. 15(a)–15(c)].

IV. DISCUSSION

From the data in the previous section we see that the interstitial gas affects the formation of the granular jet by facilitating a more fluidlike response of the bed as a whole, and through the trapped air pocket(s) which directly push sand upwards. These two effects at first glance seem unrelated, but both can be connected to the compression of interstitial gas trapped by the bed.

From Darcy's law [26,32], the gas velocity \mathbf{u} through a porous medium driven by a pressure gradient is $\mathbf{u} = -\frac{k}{\mu(1-\phi)}\nabla P$, where μ is the viscosity of the gas, and k the permeability of the bed, which is determined by the packing density ϕ and grain diameter d through the Carman-Kozeny relation [26] $k = \frac{d^2(1-\phi)^3}{180\phi^2}$. The continuity equation for the gas

flow is $\frac{\partial(\varepsilon\rho_g)}{\partial t} + \nabla \cdot (\rho_g \varepsilon \mathbf{u}) = 0$, where $\varepsilon \equiv 1 - \phi$ is the open volume fraction and ρ_g is the gas density. It is a standard procedure to assume isothermal compression of the gas, so that $\rho_g \propto P$ [33,34]. Combining the continuity equation with Darcy's law we obtain

$$\frac{\partial}{\partial t}[(1-\phi)P] = \nabla \cdot \left(P \frac{k}{\mu} \nabla P \right). \quad (1)$$

Assuming small variations in the pressure, so that $P = P_0 + \delta P$ with $\delta P/P_0 \ll 1$ and assuming a constant packing ϕ , Eq. (1) reduces to a simple diffusion equation for δP with diffusion constant $D = \frac{P_0 k}{\mu(1-\phi)}$ [26,33–35].

If the time scale for the diffusion of the gas out of the bed is significantly longer than the time scale for the granular flow, then gas trapped and compressed by the bed can create pressure differences capable of supporting the bed. The diffusion constant D varies over the range of packing densities ϕ measured in our x-ray movies, so in estimating this time scale we consider the range of packing densities from $0.49 \leq \phi \leq 0.58$. For $d=50 \mu\text{m}$, $\mu=1.8 \times 10^{-5}$ Pa s and, for the given range of packing densities, the diffusion constant D ranges between 410 and 840 cm^2/s at $P_0=101$ kPa (the value $D \sim 5 \text{ cm}^2/\text{s}$ stated in [28] is a typographical error and all other numbers in that same paper are correct for $\phi=0.55$). The time scale to diffuse across the depth of the bed (a distance $L=8.5$ cm) is $\tau_D = L^2/D$, which falls between 90 and 180 ms, significantly longer than the time $t_m \sim 30$ ms for the bed to rise to δh_{max} .

To see how the compaction of the bed increases with decreasing pressure, one must generalize the derivation of Eq. (1) to include the flow of the bed material as well as the gas flow. Describing the flow of bed material with a velocity field \mathbf{v}_{bed} , the continuity equation for the bed material is $\frac{\partial\phi}{\partial t} + \nabla \cdot (\phi \mathbf{v}_{\text{bed}}) = 0$. The gas velocity \mathbf{u} in Darcy's law is replaced by $\mathbf{u} - \mathbf{v}_{\text{bed}}$ to account for the motion of the gas relative to the bed. Combining the continuity equations for the bed and gas flow leads to the addition of a term $-P_0 \nabla \cdot \mathbf{v}_{\text{bed}}$ to the right-hand side of Eq. (1) [36,37]. Since $\nabla \cdot \mathbf{v}_{\text{bed}} = -\frac{1}{\phi} \left(\frac{\partial\phi}{\partial t} + \mathbf{v}_{\text{bed}} \cdot \nabla \phi \right)$, this new term relates changes in packing density to changes in the gas pressure. If, as before, we assume small pressure changes and neglect spatial gradients in pressure and ϕ , the equation describing the pressure changes simplifies to

$$\frac{\partial\delta P}{\partial t} = D\nabla^2\delta P + \frac{P_0}{\phi(1-\phi)} \frac{\partial\phi}{\partial t}, \quad (2)$$

which is just a diffusion equation with a source term. The source term $\frac{P_0}{\phi(1-\phi)} \frac{\partial\phi}{\partial t}$ describes how a rapid increase in packing density ϕ increases the gas pressure in the bed. Since this term is proportional to the ambient gas pressure P_0 , for large P_0 a change in packing density will correspond to a large increase in gas pressure, making it harder to compress the bed. As P_0 is decreased, the pressure change corresponding to a change in packing is smaller, making it easier for the bed to compress under the impacting sphere.

Trapped, compressed interstitial gas prevents compaction at high P_0 , so the bed flows out of the way of the sphere like an incompressible fluid and allows the sphere to open up a large cavity behind it. From the x-ray videos we see that this cavity pinches shut at two locations [Figs. 11(c)–11(e)], enclosing a large pocket of gas. If the volume of the gas pocket decreases faster than gas can escape through the porous bed, then the trapped gas can be compressed by the bed and push up on the material above it, similar to the way interstitial gas prevents compaction. We can directly measure the rate that the bottom of the gas pocket closes from the x-ray videos. At $P_0=101$ kPa the bottom of the cavity moves up with a velocity of about $v_b \sim 1$ m/s. Most of the gas flow out of the pocket will be through the plug of sand formed by the upper pinch off, which is the shortest path between the pocket and the ambient air. We use Darcy's law to approximate the flow velocity out of this plug of height s as $u_{\text{out}} \simeq \frac{k}{\mu s} \Delta P$, where ΔP is the pressure difference between the gas in the pocket and the ambient air above the bed.

For short times before the plug moves appreciably, we can estimate ΔP . In the simplest model we approximate the cavity and the plug as cylinders with a constant radius r . The bottom of the plug moves upward with a constant velocity $v_b \sim 1$ m/s, so the height of the cylindrical cavity decreases linearly with time according to $h(t)=h_0-v_b t$. Balancing the flow out of the plug with the change in the mass of air in the cavity, we have $V \frac{d\rho_g}{dt} + \rho_g \frac{dV}{dt} = -Q_{\text{out}}$. Here V is the volume of the cavity and $Q_{\text{out}} = \rho_g \pi r^2 u_{\text{out}}$ the mass flow rate out of the cavity. Solving this equation for short times, one finds the pressure difference across the plug rapidly increases according to $\Delta P \simeq P_0 t / t^*$. Here $t=0$ is the time when the top starts to pinch off and, in this simple model, $t^* = h_0 / v_b$ is the time scale for complete collapse of a cavity of initial height h_0 . The pressure difference required to support the weight of the plug is only $\Delta P_w = \rho_b \phi g s \simeq 0.13$ kPa, where $\rho_b = 2.5$ g/cm³ is the density of the bed material, g the acceleration due to gravity, and we use $\phi = 0.55$. From the x-ray movies at 101 kPa we measure $s \sim 1$ cm and $h_0 \sim 3$ cm, so a pressure difference ΔP_w capable of supporting the weight of the plug builds in less than 0.1 ms. As before, we assume isothermal compression of the gas, though numerical solutions for the pressure assuming adiabatic compression do not differ substantially over the short times considered here.

In the above estimate for the pressure in the air pocket, we have ignored diffusion of air into the rest of the bed. However, we can show that diffusion is too slow to relax ΔP significantly. A conservative lower bound for the diffusion time scale is the time for gas to diffuse just to the walls of the container, a distance $l \sim 1$ cm. This time scale $\tau_d = l^2 / D \sim 1$ ms, much longer than the time for the pressure to increase to ΔP_w . In a time τ_d the pressure difference would already have reached ~ 4 kPa or 30 times ΔP_w . Thus an overpressure capable of driving the plug upwards will develop long before outflow of air through the plug or the bed can relax the pressure gradient.

In Figs. 11(d), 11(e), 11(i), and 11(j) one indeed observes upward motion of the top surface of the air pocket even though the inertial collapse of the beds walls should result in a downward moving surface [21]. This suggests that there

must be an overpressure in the cavity. The velocity of this upward motion at 101 kPa is about 0.4 m/s, which is comparable to the velocity of a tracer particle entrained in the jet [Fig. 12(d)]. Though we cannot directly measure the pressure in the cavity, this strongly suggests that the pressure in the cavity is pushing on the sand above it.

As P_0 is decreased, there is less interstitial gas and its effect is decreased. This is seen directly in our simple model for the pressurization of the trapped gas pocket, where the pressure difference across the upper plug scales as $\Delta P \propto P_0$.

A notable feature of this scenario for jet formation is that, despite the jet formation being strongly affected by the presence of interstitial gas, the density of the gas plays no role. This is in agreement with our measurements of the jet height in SF₆ (Fig. 10). Instead, the permeability of the bed plays the key role by determining the time scale for gas to diffuse through the bed. The permeability depends on the grain diameter according to $k \sim d^2$, so the effect of air is much less pronounced with larger grains. This is consistent with the large reduction in the jet with increasing grain diameter found by [16] with d up to 275 μm and in our experiment with 1 mm grains (Fig. 9).

The importance of interstitial air is also reflected in the subsurface velocity of the impacting object, since gas will only be trapped if the diffusion time scale is longer than time scale for the flow. We believe this is why the results reported in [15] did not show a difference in trajectories taken at atmospheric pressure and vacuum for a sphere released from $H_{\text{drop}} = 3.5$ cm (impact velocity $v_0 \sim 80$ cm/s) into beds with grain diameters 100 μm or larger. Since smaller spheres decelerate more rapidly [15] one also would expect air to play a less pronounced role as the sphere diameter is decreased. This is consistent with the disappearance of the thick jet with smaller spheres shown in Fig. 7.

Our description of the role of interstitial air in reducing the drag on the impacting sphere differs from the explanation suggested by the Twente group in [27], which attributes the reduced drag to local fluidization of the grains produced by air flow around the sphere. Our x-ray measurements of the local packing density show no evidence of decompaction in front of the advancing sphere at high pressures. If anything, we observed compaction ahead of the sphere. This effect becomes clearly visible at reduced pressures where it extends significant distances in front of the leading edge of the sphere, similar to material build-up in front of a snow plow or bulldozer [14]. Furthermore, we find a uniform rise of the bed across the whole container for $D_s \geq 1.0$ cm and $H_{\text{drop}} \geq 40$ cm, and similar behavior was also reported in [27]. Taken together this demonstrates that dynamical effects mediated by the interstitial air are not confined to a small local region around the moving sphere. Instead, the bed as a whole responds like an incompressible fluid if the pressure of interstitial gas is close to atmospheric conditions (Figs. 8 and 13).

The Twente group attributes the reduced jet height at lower pressure to the reduced penetration depth. For a sphere diameter $D_s = 1.6$ cm and a range of drop heights ($H_{\text{drop}} = 2.8$ –52.8 cm) they also did not observe the thick-thin jet structure and point to the possibility that this structure may be the result of a boundary effect. Though boundaries likely influence the flow of the bed material, our results show that

the thick-thin jet structure is not a product of nearby container walls. The thick jet is still observed even when $D_s = 1$ cm, a factor of 14 smaller than the container diameter, and the width of the thick jet monotonically decreases with D_s (Fig. 7). We also see little difference between the jets in 14- and 3.5-cm-diameter containers for otherwise similar conditions. We instead attribute the disappearance of the thick jet with small spheres and low release heights to the lower velocity of the sphere and, therefore, earlier closure time for the cavity which prevents the formation of a large pressurized gas pocket. Our subsurface radiography results confirm that gravity-driven cavity collapse, as originally proposed by the Twente group, is essential for understanding the initial stages of jet formation. However, we find that this gravity-driven collapse produces only a thin jet (Fig. 11). To understand the emergence of the thick jet, i.e., the second stage of the overall jet structure (Figs. 1 and 7), and its dependence on pressure it is essential to consider also the gas trapped inside the cavity as well as inside the interstitial spaces between the particles.

The absence of compaction at atmospheric pressure is accompanied by a much less dissipative, fluidlike flow of the bed (Figs. 13 and 14). This suggests that the trapped interstitial gas which prevents compaction also reduces energy dissipation by inelastic grain-grain collisions. This is seen both in measurements of potential energy gained by the bed as it rises, and by direct measurements of the potential energy of the jet [Fig. 8(b) and [28]]. The scaling of the jet energy with the impact energy observed at atmospheric pressure has also been observed in liquid jets, despite the differences in the formation of the two jets [20].

V. CONCLUSIONS

Our results demonstrate how the dynamic gas-grain coupling can determine the fluidlike properties of a loose, fine-grained granular bed. The low permeability of the bed traps interstitial gas in the bed, which in turn prevents compaction. The incompressible fluidlike flow observed at high ambient pressures is much more elastic, with a larger fraction of the impact energy transferred to the jet. This is presumably due to a reduction in the energy lost to in-elastic grain-grain collisions because of the reduced compaction. The interaction between grains and trapped gas can also lead to qualitatively new phenomena in granular flows, such as the gas-driven thick jet. This demonstrates that single-fluid models of the granular bed cannot capture the full range of observed behavior.

The importance of ambient gas in fine-grained beds also limits the applicability of models for the drag force obtained from measurements in larger grained beds. Though a unified force law has recently been proposed to encompass a wide range of data on low-speed impacts in beds with grain diameters $>200 \mu\text{m}$ [15], in fine grains the dynamics are more complex. In addition to the ambient pressure, the initial packing also can play an important role, as described in [7]. With an initially dense-packed bed, the bed will have to dilate for the sphere to pass through. In our model changes in the bed packing density are opposed by the interstitial gas;

therefore, unless the system is evacuated, the presence of ambient gas counteracts both compaction and dilation. This suggests that in sufficiently dense beds, the ambient gas should play a role that is the reverse of what we discussed here for loose beds: inhibiting the penetration of the impacting sphere by preventing the dilation of the bed.

While this work explored the initiation of a granular jet by an impacting sphere and its subsequent growth, there are several aspects that remain unresolved. One of these concerns is the mechanism that sets the jet's remarkably sharp boundaries. Radial collapse of the cavity produced by the sphere will produce net momentum flux along the vertical axis of symmetry, resulting in jets both upward and downward, as observed. Additional upward momentum introduced by the compressed air pocket will skew this balance in favor of a large upward jet; but it is surprising that these net momenta are near-perfectly balanced with respect to fluctuations in both radial and longitudinal directions, especially since they are the result of collisions between macroscopic particles rather than molecules in an ordinary fluid. The fluidlike character of the granular jet emerging from such collisions is reminiscent of the sharply defined sheet of grains which emerges after a stream of grains hits a stationary target and which closely resembles the water bells observed for fluid streams [38]. This target effectively plays the role of a mirror and the same behavior is observed for two streams colliding head-on. The sharpness of this sheet is set by the number density of particles in a narrow collision region in front of the flat target. In the case of the granular jet discussed here, the collision region is the cylindrical region below the bed surface where the cavity pinches off. Thus the jet might be thought of as a tightly rolled up sheet or, effectively, as the one-dimensional analog of the two-dimensional ejecta observed in [33]. Intriguingly, cooperative fluidlike behavior that manifests itself in the sheets emerges as long as the stream cross section in the collision region is larger than 10–50 particles across. Because the collision region for the granular jets involves a volume determined not simply by the cavity diameter but also by the depth over which pinch-off occurs, this suggests that well-defined, fluidlike jets should be observable even for small sphere diameters or larger grains, in line with our observations [Figs. 7 and 9(d)].

The jet also remains remarkably sharp during its long rise above the bed, and even maintains bends and kinks such those shown in Fig. 7. This is possible only if there is very little internal grain motion, so that all the grains are moving in the same direction with the same velocity. Using the common definition of a kinetic granular temperature as the mean square of the velocity fluctuations [39,40], the jet, once formed, can be thought of as a dense, ultracold gas.

A related issue is the final breakup of the jet into particle clusters. This can be seen already before the jet reaches its maximum height. Studies focusing on the breakup of a freely falling granular stream found that the cluster formation is not initiated by the ambient gas, but could not separate the roles of grain inelasticity and cohesion [41]. Although our results enable an understanding of the mechanisms behind the birth of a granular jet, the death of the jet as falling clusters of grains requires further investigation.

ACKNOWLEDGMENTS

We thank X. Cheng, B. Cooper, K. Foster, N. Keim, M. Möbius, S. Nagel, and W. Zhang for insightful discussions. This work was supported by NSF through its MRSEC program under Grant No. DMR-02137452 and by DOD/AFOSR Grant No. FA9550-07-101459. Portions of this work were performed at GeoSoilEnviroCARS (Sector 13), Advanced

Photon Source (APS), Argonne National Laboratory. GeoSoilEnviroCARS is supported by the National Science Foundation -Earth Sciences (Grant No. EAR-0622171) and Department of Energy—Geo-sciences (Grant No. DE-FG02-94ER14466). Use of the Advanced Photon Source was supported by the U. S. Department of Energy, Office of Science, Office of Basic Energy Sciences, under Contract No. DE-AC02-06CH11357.

-
- [1] B. Robins, *New Principles of Gunnery* (J. Nourse, London, 1742).
- [2] J. V. Poncelet, *Introduction à la Mécanique Industrielle, Physique ou Expérimentale* (Gauthier-Villars, Paris, 1839).
- [3] H. M. Jaeger, S. R. Nagel, and R. P. Behringer, *Rev. Mod. Phys.* **68**, 1259 (1996).
- [4] R. L. Geer, Technical Report No. ASD TR 61-595, Wright-Patterson AFB, Ohio, 1962.
- [5] D. J. Roddy, J. B. Rittenhouse, and R. F. Scott, *AIAA J.* **1**, 868 (1963).
- [6] E. C. Bennett, R. F. Scott, L. D. Jaffe, E. P. Frink, and H. E. Martens, Technical Report 32–326, Jet Propulsion Laboratory, California Institute of Technology, 1963.
- [7] L. V. Clark and J. L. McCarty, Technical Note D-1519, NASA, Langley Research Center, 1963.
- [8] M. P. Ciamarra, A. H. Lara, A. T. Lee, D. I. Goldman, I. Vishik, and H. L. Swinney, *Phys. Rev. Lett.* **92**, 194301 (2004).
- [9] K. E. Daniels, J. E. Coppock, and R. P. Behringer, *Chaos* **14**, s4 (2004).
- [10] A. M. Walsh, K. E. Holloway, P. Habdas, and J. R. de Bruyn, *Phys. Rev. Lett.* **91**, 104301 (2003).
- [11] J. R. de Bruyn and A. M. Walsh, *Can. J. Phys.* **82**, 439 (2004).
- [12] D. Lohse, R. Rauhé, R. Bergmann, and D. van der Meer, *Nature (London)* **432**, 689 (2004).
- [13] M. A. Ambroso, R. D. Kamien, and D. J. Durian, *Phys. Rev. E* **72**, 041305 (2005).
- [14] L. S. Tsimring and D. Volfson, in *Powders and Grains 2005*, edited by R. Garcia-Rojo, H. J. Herrmann, and S. McNamara (Balkema, Rotterdam, 2005), p. 1215.
- [15] H. Katsuragi and D. J. Durian, *Nat. Phys.* **3**, 420 (2007).
- [16] S. T. Thoroddsen and A. Q. Shen, *Phys. Fluids* **13**, 4 (2001).
- [17] A. M. Worthington, *A Study of Splashes* (Longmans and Green, London, 1908).
- [18] B. W. Zeff, B. Kleber, J. Fineberg, and D. P. Lathrop, *Nature (London)* **403**, 401 (2000).
- [19] J. E. Hogrefe, N. L. Peffley, C. L. Goodridge, W. T. Shi, H. G. E. Hentschel, and D. P. Lathrop, *Physica D* **123**, 183 (1998).
- [20] A. I. Fedorchenko and A.-B. Wang, *Phys. Fluids* **16**, 1349 (2004).
- [21] D. Lohse, R. Bergmann, R. Mikkelsen, C. Zeilstra, D. van der Meer, M. Versluis, K. van der Weele, M. van der Hoef, and H. Kuipers, *Phys. Rev. Lett.* **93**, 198003 (2004).
- [22] J. R. Royer, E. I. Corwin, A. Flior, M.-L. Cordero, M. L. Rivers, P. J. Eng, and H. M. Jaeger, *Nat. Phys.* **1**, 164 (2005).
- [23] S. V. Bulychov, D. V. Vyalykh, A. E. Dubinov, I. L. L'vov, S. A. Sadovoi, and V. D. Selemir, *Instrum. Exp. Tech.* **49**, 568 (2006).
- [24] S. V. Bulychov, D. V. Vyalykh, A. E. Dubinov, I. L. L'vov, S. A. Sadovoi, and V. D. Selemir, *Dokl. Phys.* **51**, 486 (2006).
- [25] M. Hou, Z. Peng, R. Liu, K. Lu, and C. K. Chan, *Phys. Rev. E* **72**, 062301 (2005).
- [26] P. C. Carman, *Flow of Gases Through Porous Media* (Butterworths Scientific, London, 1956).
- [27] G. Caballero, R. Bergmann, D. van der Meer, A. Prosperetti, and D. Lohse, *Phys. Rev. Lett.* **99**, 018001 (2007).
- [28] J. R. Royer, E. I. Corwin, P. J. Eng, and H. M. Jaeger, *Phys. Rev. Lett.* **99**, 038003 (2007).
- [29] T. Shinbrot, K. LaMarche, and B. J. Glasser, *Phys. Rev. Lett.* **96**, 178002 (2006).
- [30] M. Bigas, E. Cabruja, J. Forest, and J. Salvi, *Microelectron. J.* **37**, 433 (2006).
- [31] See EPAPS Document No. E-PLLEE8-78-105807 for composite x-ray movies showing the impact of a $D_s=12$ mm sphere at $P_0=101$ kPa (101kPa12mm.mov), 12 kPa (12kPa12mm.mov), 0.7 kPa (07kPa12mm.mov), and for a $D_s=6$ mm sphere at 101 kPa (101kPa6mm.mov). For more information on EPAPS, see <http://www.aip.org/pubservs/epaps.html>.
- [32] H. P. G. Darcy, *Les Fontaines Publiques de la Ville de Dijon* (Victor Dalmont, Paris, 1856).
- [33] R. G. Gutman and J. F. Davidson, *Chem. Eng. Sci.* **30**, 89 (1975).
- [34] H. K. Pak, E. Van Doorn, and R. P. Behringer, *Phys. Rev. Lett.* **74**, 4643 (1995).
- [35] M. E. Möbius, X. Cheng, P. Eshuis, G. S. Karczmar, S. R. Nagel, and H. M. Jaeger, *Phys. Rev. E* **72**, 011304 (2005).
- [36] S. McNamara, E. G. Flekkøy, and K. J. Måløy, *Phys. Rev. E* **61**, 4054 (2000).
- [37] D.-V. Anghel, M. Strauss, S. McNamara, E. G. Flekkoy, and K. J. Maloy, *Phys. Rev. E* **74**, 029906 (2006).
- [38] X. Cheng, G. Varas, D. Citron, H. M. Jaeger, and S. R. Nagel, *Phys. Rev. Lett.* **99**, 188001 (2007).
- [39] S. Ogawa, in *Proceedings of the US-Japan Seminar on Continuum-Mechanical and Statistical Approaches in the Mechanics of Granular Materials* (Gukujutsu Bunken Fukuyukai, Tokyo, 1978), pp. 208–217.
- [40] C. S. Campbell, *Annu. Rev. Fluid Mech.* **22**, 57 (1990).
- [41] M. E. Möbius, *Phys. Rev. E* **74**, 051304 (2006).